ROBUSTNESS OF TIME-RESOLVED MEASUREMENT TO UNKNOWN AND VARIABLE BEAM CURRENT IN PARTICLE BEAM MICROSCOPY

Luisa Watkins[1], *Sheila W. Seidel*[1,2], *Minxu Peng*[1], *Akshay Agarwal*[3], *Christopher C. Yu*[2], *and Vivek K Goyal*[1]

Boston University[1], Charles Stark Draper Laboratory[2], Massachusetts Institute of Technology[3]

ABSTRACT

Variations in the intensity of the incident beam can cause significant inaccuracies in microscopes that use focused beams of electrons or ions. Existing mitigation methods depend on the artifacts having characteristic spatial structures explained by the raster scan pattern and temporal correlation of the beam current variations. We show that recently introduced time-resolved measurement methods create robustness to beam current variations that improve significantly upon existing methods while not depending on separability of artifact structure from underlying image content. These advantages are illustrated through Monte Carlo simulations representative of both helium ion microscopy (higher secondary electron yield) and scanning electron microscopy (lower secondary electron yield). Notably, this demonstrates that when the beam current variation is appreciable, time-resolved measurements provide a novel benefit in particle beam microscopy that extends to low secondary electron yields.

***Index Terms*—** Computational imaging, focused ion beam microscopy, helium ion microscopy, Poisson processes, scanning electron microscopy.

1. INTRODUCTION

Particle beam microscopes image samples using a focused beam of charged particles. The helium ion microscope (HIM) offers several exciting advantages over other instruments, including high secondary electron (SE) yield, large depth of field, and sub-nanometer resolution [1–3]. Like the more prevalent scanning electron microscope (SEM), the quality of the HIM micrograph depends heavily on the ability of the instrument to maintain a stable beam current. In practice, the beam emitted by a gas field ion source (GFIS) in an HIM may vary as a result of contamination [4]. When a sample is raster scanned row by row, this beam current variation gives rise to horizontal stripe artifacts in the resulting micrograph, as illustrated in the second column of Fig. 3. Furthermore, as the GFIS tip ages, the beam current may also drop below the manufacturer's rated value. An unstable GFIS may be 'reset' by baking the source components (i.e., heating to extraordinarily high temperatures to drive out gas contaminants) [2], but this process can cost a laboratory days of use of an expensive instrument. Thus, a computational remedy for variable or unknown beam current would be valuable.

A simple existing method to address beam current variation is so-called 'line averaging' or 'frame averaging,' where a line or frame is scanned repeatedly and the resulting measurements are averaged [2, 5]. This reduces striping artifacts because the beam current variations are averaged over multiple visits to each pixel. However, these methods increase the sensitivity to sample drift, i.e., motion of the sample between scans, and some collection time efficiency is lost by the additional beam scanning. A second class of mitigation techniques applies image processing tools to remove striped content from the micrograph; for example, in [5, 6], image content with low horizontal frequency is removed. Because these methods are designed to remove stripes, they have also been applied to remove 'curtaining' artifacts that arise from variations in an ion beam's milling rate [7, 8]. Though undesired, curtaining arises from accurate representation of the sample. In contrast, beam current artifacts are due to the data processing algorithms' failure to account for the *true* beam current; they do not represent the underlying sample.

In this paper, we introduce and evaluate a new approach to mitigating beam current variation that depends on neither temporal correlation of the beam current nor on a resulting spatial structure in the artifacts. We show that insensitivity to beam current is a property of an approach to data collection and analysis that was recently introduced solely to improve estimation of SE yield when the beam current is known precisely [9]. A typical particle beam microscopy system raster scans a beam across a sample, measuring the SEs expelled from the surface in response. At each pixel, over dwell time t, the total number of SEs generate a *single* measurement that is mapped to a grayscale level to form an image of the sample. With the *time-resolved* (TR) measurement introduced in [9], the per-pixel dwell time is divided into n sub-acquisitions of length t/n, and the number of SEs is measured separately for each. Estimators proposed in [9, 10] combine these n measurements to form higher fidelity images without having changed the ion dose or the order in which pixels are visited. In [11], SE yield estimation from [9] is combined with estimation of unknown beam current. In this work, we demonstrate that the techniques in [9] alone are robust to unknown and variable beam current, even outperforming existing mitigation techniques based on image filtering [5, 6]. Section 2 reviews the concepts of time-resolved sensing introduced in [9]. Section 3 contains a sensitivity analysis which illustrates the reduced sensitivity of our methods to error in the assumed beam current. In Section 4, we use synthetic data to show that in the presence of time-varying beam current, our methods improve upon existing techniques.

2. MEASUREMENT MODELS AND IMAGE FORMATION

In this section, we present measurement models for particle beam microscopy with direct detection of SEs. For simplicity, we refer to incident particles as ions, though the models apply to both SEM and focused ion beam (FIB) microscopy. While direct detection is not currently prevalent in commercial SEM and FIB microscopes, it offers higher signal-to-noise ratio than systems with scintillators and

This work was supported in part by a Boston University Clare Boothe Luce Scholar Award, a Draper Laboratory Fellowship, and the US National Science Foundation under Grant No. 1815896.

photomultiplier tubes [12–14]. Direct detection is easier to model, and the advantages of time-resolved sensing are presumably not dependent on the use of direct detection [10]. Since we do not consider spatial regularization, we omit any pixel indexing. Where applicable, the dependence of estimators on an assumed beam current parameter λ is emphasized in the notation; all estimators depend on the measured data, so this is omitted from the notation.

An incident beam is well-modeled as a Poisson process [15], so at a single pixel, the number of incident ions M over dwell time t is a Poisson random variable with mean $\lambda = \Lambda t$, where Λ is the rate of incident ions per unit time. The number of SEs expelled by the ith incident ion, X_i, can also be described as a Poisson random variable: $X_i \sim \text{Poisson}(\eta)$, where mean η is the SE yield. The total number of detected SEs, $Y = \sum_{i=1}^{M} X_i$, is the single measurement conventionally used to produce an estimate of η. Under this model, Y is a compound Poisson random variable with the *Neyman Type A* distribution and a probability mass function (PMF) given by

$$P_Y(\mathrm{y}; \eta, \lambda) = \frac{e^{-\lambda}\eta^{\mathrm{y}}}{\mathrm{y}!} \sum_{m=0}^{\infty} \frac{(\lambda e^{-\eta}) m^{\mathrm{y}}}{m!}. \tag{1}$$

Assuming λ is known, the estimator $\widehat{\eta}_{\text{baseline}}(\lambda) = Y/\lambda$ is unbiased and has mean-squared error (MSE) $(\eta + \eta^2)/\lambda$.

With time-resolved measurement, dwell time t is split into n sub-acquisitions yielding measurements: Y_1, Y_2, …, Y_n. Given short enough sub-acquisitions (i.e., large n), the dose λ/n becomes small enough that observing more than one incident ion in one sub-acquisition is unlikely. Assuming η is large enough that most incident ions result in at least 1 SE, the number of sub-acquisitions where the number of observed SEs is strictly positive is also roughly the number of incident ions: $M \approx \sum_{k=1}^{n} \mathbb{1}_{\{Y_k > 0\}}$, where $\mathbb{1}_{\{Y_k>0\}}$ is the indicator function of $\{Y_k > 0\}$. The *quotient mode* (QM) estimator proposed in [9] is inspired this insight:

$$\widehat{\eta}_{\text{QM}} = \frac{Y_1 + Y_2 + \cdots + Y_n}{\sum_{k=1}^{n} \mathbb{1}_{\{Y_k>0\}}}. \tag{2}$$

Although $\widehat{\eta}_{\text{QM}}$ is similar to $\widehat{\eta}_{\text{baseline}}$ in that the numerator is a sum of M random variables with mean η, it generally outperforms $\widehat{\eta}_{\text{baseline}}$ because its denominator is a better proxy for M. A similar concept for instruments without direct detection of SEs appears in [16, 17].

When SE yield η is low, incident ions will less reliably result in at least 1 SE. In this case, $\sum_{k=1}^{n} \mathbb{1}_{\{Y_k>0\}}$ will be significantly smaller than the true number of incident ions, leading to a large bias in $\widehat{\eta}_{\text{QM}}$. The probability of an incident ion expelling at least 1 SE is $1 - e^{-\eta}$, so if η were known, our estimate of the number incident ions could be adjusted: $(1-e^{-\eta})^{-1} \sum_{k=1}^{n} \mathbb{1}_{\{Y_k>0\}}$. Given that η is not known, using this improved estimate for M as the denominator in (2) results in a transcendental equation, of which the closed form solution yields the *Lambert quotient mode* (LQM) estimator:

$$\widehat{\eta}_{\text{LQM}} = W(-\widehat{\eta}_{\text{QM}} e^{-\widehat{\eta}_{\text{QM}}}) + \widehat{\eta}_{\text{QM}}, \tag{3}$$

where $W(\cdot)$ is the Lambert W function [18]. Note that (2) and (3) are computed without any knowledge of λ.

The joint PMF of the time-resolved measurements is

$$P_{Y_1,\ldots,Y_n}(y_1, \ldots, y_n; \eta, \lambda) = \prod_{k=1}^{n} P_Y(\mathrm{y}_k; \eta, \lambda/n), \tag{4}$$

where $P_Y(\cdot;\cdot,\cdot)$ is given by (1). We refer to the maximizer over η as the *time-resolved maximum likelihood* (TRML) estimate $\widehat{\eta}_{\text{TRML}}(\lambda)$. Since the decision variable is scalar, this optimization may be performed using a grid search.

3. SENSITIVITY TO UNKNOWN BEAM CURRENT

Consider a pixel with true incident dose λ, and denote the dose assumed by an estimator by $\widetilde{\lambda} = \lambda(1 + \epsilon)$. When ϵ is nonzero, the estimator is mismatched, as when the dose varies stochastically or does not match the instrument setting. In this section, we examine the bias, variance, and MSE of mismatched estimators.

The mismatched baseline estimate $\widehat{\eta}_{\text{baseline}}(\widetilde{\lambda}) = Y/(\lambda(1 + \epsilon))$ has mean $\eta/(1 + \epsilon)$ and variance $(\eta + \eta^2)/[\lambda(1 + \epsilon)^2]$. It follows that its bias is $\eta\epsilon/(1 + \epsilon)$ and its MSE is

$$\text{MSE}\big(\widehat{\eta}_{\text{baseline}}(\widetilde{\lambda})\big) = \eta^2 \Big(\frac{\epsilon}{1+\epsilon}\Big)^2 + \frac{\eta + \eta^2}{\lambda(1+\epsilon)^2}. \tag{5}$$

The bias, variance, and MSE of $\widehat{\eta}_{\text{baseline}}(\widetilde{\lambda})$ as functions of ϵ are plotted in Figure 1 along with empirical values for $\widehat{\eta}_{\text{QM}}$, $\widehat{\eta}_{\text{LQM}}$, and $\widehat{\eta}_{\text{TRML}}(\widetilde{\lambda})$ for parameters $\eta = 5$, $\lambda = 20$, and $n = 200$. As noted earlier, $\widehat{\eta}_{\text{QM}}$ and $\widehat{\eta}_{\text{LQM}}$ do not depend on a dose parameter, so they have no dependence on ϵ. For the dose used in Figure 1, these two estimators achieve lower MSE with *no* knowledge of λ than the baseline estimator does with *perfect* knowledge. The more complex estimator $\widehat{\eta}_{\text{TRML}}$ has some dependence on ϵ, but far less than the baseline estimator. It has lower MSE than the baseline estimator for all the considered values of ϵ, but it does become worse than the QM and LQM estimators at large enough ϵ.

One of the merits of the baseline estimator is its zero bias when there is no mismatch, combined with variance that vanishes with increasing dose λ. Thus, it could outperform more sophisticated estimators at large enough dose λ if the other estimators have nonzero asymptotic bias. Figure 2 illustrates this phenomenon along with the dominance of bias in the mismatched case. We plot the MSE of each estimator as a function of total dose λ, maintaining $\lambda/n = 0.1$ from Figure 1, considering $\eta \in \{1, 5\}$, for the cases of $\epsilon = 0$ and $\epsilon = 0.2$. (Since QM and LQM estimators do not depend on a dose parameter, each has only one curve on each graph.) With no mismatch ($\epsilon = 0$), the MSE of the baseline estimator exhibits an exact $1/\lambda$ behavior (slope -1 on this log–log plot), and $\widehat{\eta}_{\text{TRML}}$ follows, with an improvement factor of $(1 + \eta)(1 - \eta e^{-\eta})$ as predicted by [10], up to large λ, where the small bias of $\widehat{\eta}_{\text{TRML}}$ eventually dominates. With mismatch ($\epsilon = 0.2$), bias dominates at much lower values of λ; very large improvements over the baseline estimator are possible. In Figure 2a, we see the very poor performance of $\widehat{\eta}_{\text{QM}}$ for small values of η (due to bias that inspires the definition of the LQM estimator) and that $\widehat{\eta}_{\text{LQM}}$ can have lower MSE than $\widehat{\eta}_{\text{TRML}}$ with moderate mismatch and doses that are high but not necessarily unreasonable. The asymptotes of the QM estimator MSEs in Figure 2 match the square of the limit as $\lambda \to \infty$ of the expression for bias derived in [10].

4. MICROSCOPY SIMULATIONS

The results in the previous section show that processing of time-resolved measurements provides the potential for great robustness to mismatch between an instrument's beam current setting—which would presumably be used in any interpretation of the data—and the actual beam current. We now illustrate this through simulated particle beam microscopy experiments. Though the TR estimators do not depend on the beam current fluctuating slowly, we construct our experiments as such since the state-of-the-art method for comparison [5] depends on striping artifacts.

Figure 3 includes five test examples. Synthetic data was produced using existing micrographs [19–22] as ground truth images.

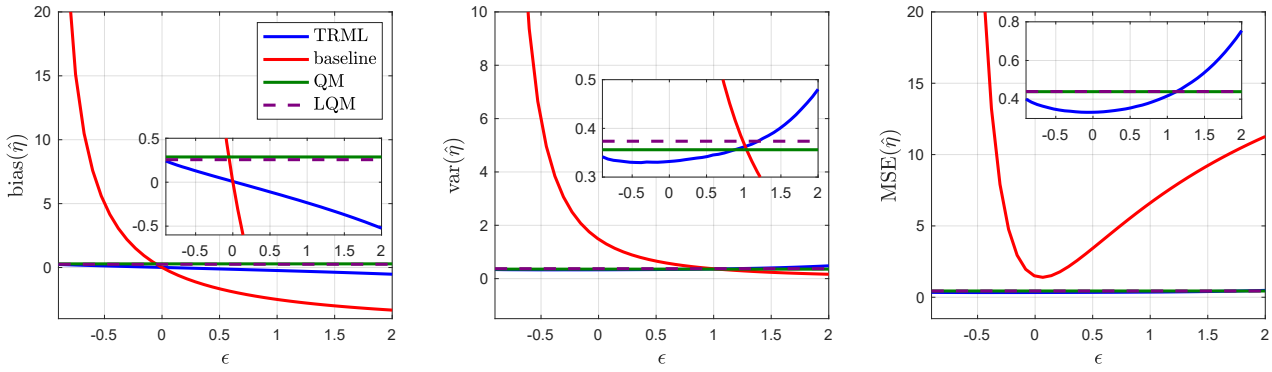

(a) Bias across ϵ (b) Variance across ϵ (c) MSE across ϵ

Fig. 1: Bias, variance, and MSE of $\hat{\eta}$ as a function of ϵ when $\eta = 5$, $\lambda = 20$, and $n = 200$.

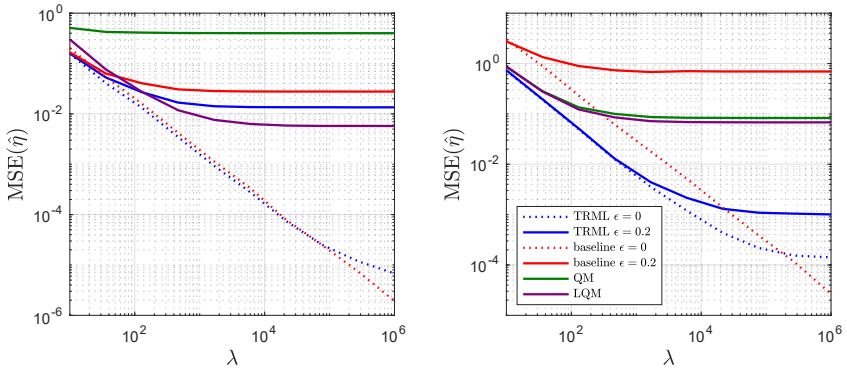

(a) $\eta = 1$ (b) $\eta = 5$

Fig. 2: MSE of $\hat{\eta}$ as a function of total dose λ when $\lambda/n = 0.1$. Note the log–log scale.

In Examples 1, 2, and 3, the images are scaled for $\eta \in [2, 8]$ to represent realistic HIM conditions [23]. In Example 4, $\eta \in [0.6, 2]$, which matches the SE yield in SEM at the maximizing electron energy, neglecting topographical effects [24]. In Example 5, $\eta \in [0.2, 1]$ for a more challenging SEM-like setting. Beam current time series were generated using a Gaussian first-order autoregressive model with parameters selected to achieve a mean dose $\tilde{\lambda}$. Inspired by Figure 2, we evaluate $\widehat{\eta}_{\mathrm{TRML}}(\tilde{\lambda})$ for the higher η scenarios (Examples 1, 2, and 3) and $\widehat{\eta}_{\mathrm{LQM}}$ for the lower η scenarios (Examples 4 and 5). In each example, we also compute the TRML estimate as if the true beam current were known: $\widehat{\eta}_{\mathrm{oracle}} = \widehat{\eta}_{\mathrm{TRML}}(\lambda)$. We compare our methods to the baseline estimator $\widehat{\eta}_{\mathrm{baseline}}$ as well as to $\widehat{\eta}_{\mathrm{FT}}$, a Fourier-domain filtering method that appears to be the state of the art [5]. In each application of $\widehat{\eta}_{\mathrm{FT}}$, we choose the coefficients to null to minimize MSE, even though this is not possible in practice due to lack of access to ground truth. Unlike $\widehat{\eta}_{\mathrm{FT}}$, our methods do not rely on the spatial structure of the artifacts and can remove artifacts without introducing new ones.

Table 1 summarizes the MSEs of the examples presented in Figure 3 through a metric we call excess MSE. It refers to the MSE beyond that of $\widehat{\eta}_{\mathrm{oracle}}$: $\mathrm{MSE}_{\mathrm{excess}}(\hat{\eta}) = \mathrm{MSE}(\hat{\eta}) - \mathrm{MSE}(\widehat{\eta}_{\mathrm{oracle}})$. Excess MSE % normalizes excess MSE by the excess MSE of $\widehat{\eta}_{\mathrm{baseline}}$. Comparison of excess MSE % values shows that in the HIM-like settings (Examples 1, 2, and 3), $\widehat{\eta}_{\mathrm{TRML}}$ comes very close to oracle performance. In the SEM-like settings (Examples 4 and 5), the reduction in excess MSE is still substantial.

Ex.	Excess MSE			Excess MSE %		
	$\widehat{\eta}_{\mathrm{baseline}}$	$\widehat{\eta}_{\mathrm{FT}}$	$\widehat{\eta}_{\mathrm{TRML}}$	$\widehat{\eta}_{\mathrm{baseline}}$	$\widehat{\eta}_{\mathrm{FT}}$	$\widehat{\eta}_{\mathrm{TRML}}$
1	1.4506	0.8572	0.0143	100	59.1	1.0
2	2.0387	0.8875	0.0845	100	43.5	4.1
3	1.1242	0.7926	0.0265	100	70.5	2.4
4	0.0484	0.0087	0.0072	100	18.0	14.9
5	0.0149	0.0039	0.0031	100	26.2	20.8

Table 1: Summary of numerical results.

5. CONCLUSION

Time-resolved measurements have already shown their potential to mitigate source shot noise in particle beam microscopy in the idealized setting of known beam current. In this work, we have demonstrated that these methods create remarkable robustness to unknown and variable beam current. Our simulations demonstrate that even with beam current varying 30% from the intended value, time-resolved methods result in lower image MSE then existing computational artifact mitigation techniques. These findings suggest computational methods could relax the requirement for a stable beam current, addressing a major limiting factor in HIM.

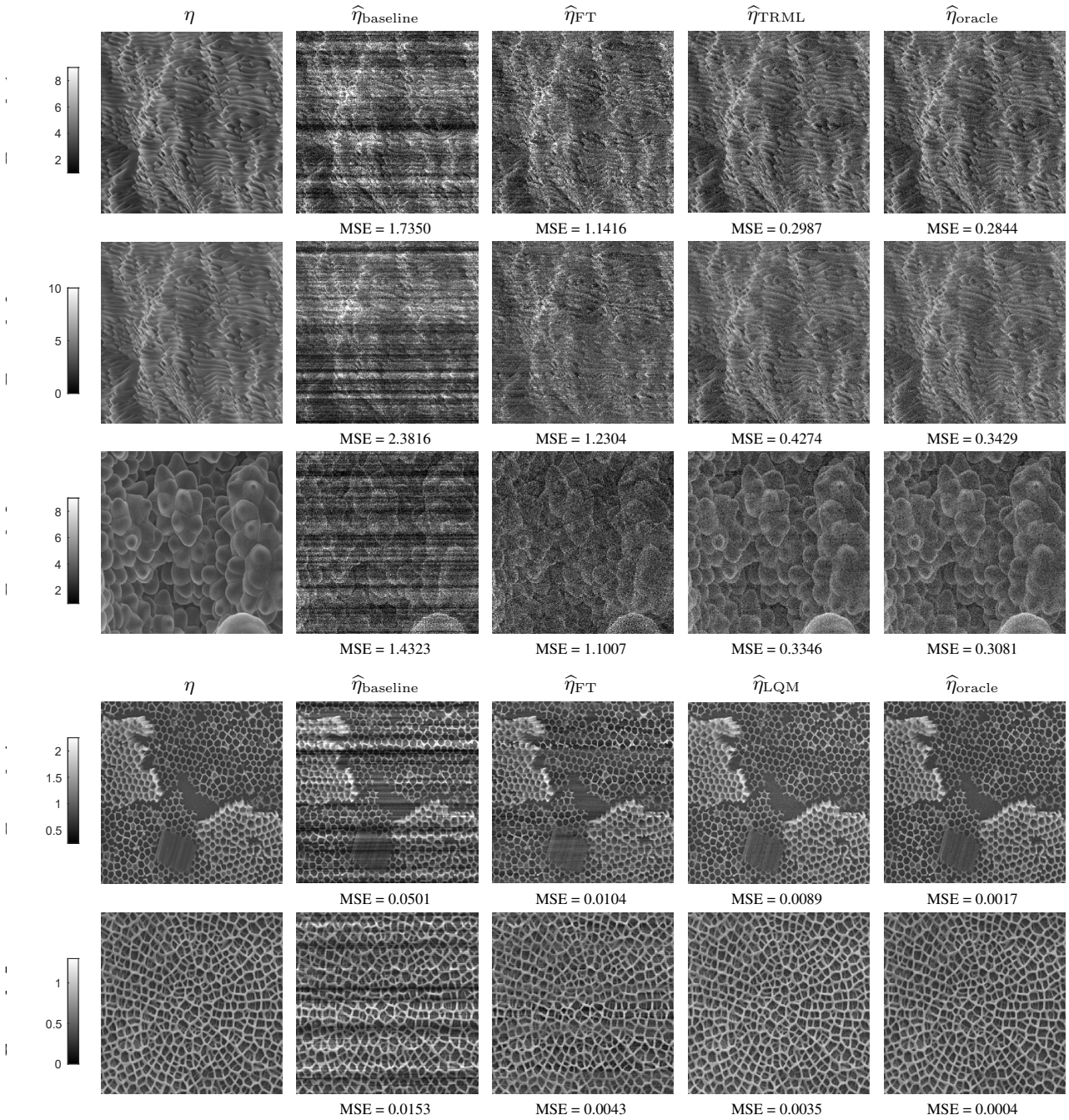

Fig. 3: Comparison of $\widehat{\eta}_{\mathrm{baseline}}$, $\widehat{\eta}_{\mathrm{FT}}$, $\widehat{\eta}_{\mathrm{TRML}}$, $\widehat{\eta}_{\mathrm{LQM}}$, and $\widehat{\eta}_{\mathrm{oracle}}$ for 5 test examples, all with nominal subacquisition dose $\tilde{\lambda}/n = 0.1$. The actual dose λ is a Gaussian autoregressive process with correlation coefficent of 0.999 for neighboring pixels in a row and standard deviation σ_λ. *Example 1*: HIM with $\eta \in [2, 8]$, $\tilde{\lambda} = 20$, and $\sigma_\lambda/\tilde{\lambda} = 0.2$. *Example 2*: HIM with $\eta \in [2, 8]$, $\tilde{\lambda} = 20$, and $\sigma_\lambda/\tilde{\lambda} = 0.3$. *Example 3*: HIM with $\eta \in [2, 8]$, $\tilde{\lambda} = 20$, and $\sigma_\lambda/\tilde{\lambda} = 0.2$. *Example 4*: SEM with $\eta \in [0.6, 2]$, $\tilde{\lambda} = 1000$, and $\sigma_\lambda/\tilde{\lambda} = 0.2$. *Example 5*: SEM with $\eta \in [0.2, 1]$, $\tilde{\lambda} = 2000$, and $\sigma_\lambda/\tilde{\lambda} = 0.2$. To improve legibility, some saturation is allowed; color bars are set so that no more than 2% of pixels are saturated in a given image.

6. REFERENCES

[1] Bill W. Ward, John A. Notte, and Nicholas P. Economou, "Helium ion microscope: A new tool for nanoscale microscopy and metrology," *J. Vac. Sci. & Technol. B*, vol. 24, no. 6, pp. 2871–2874, Nov. 2006.

[2] John Notte and Jason Huang, *The Helium Ion Microscope*, pp. 3–30, Springer International Publishing, Cham, 2016.

[3] John Morgan, John Notte, Raymond Hill, and Bill Ward, "An introduction to the helium ion microscope," *Microscopy Today*, vol. 14, no. 4, pp. 24–31, 2006.

[4] FHM F. Rahman, John A. Notte, Richard H. Livengood, and Shida Tan, "Observation of synchronized atomic motions in the field ion microscope," *Ultramicroscopy*, vol. 126, pp. 10–18, 2013.

[5] Anders J. Barlow, Jose F. Portoles, Naoko Sano, and Peter J. Cumpson, "Removing beam current artifacts in helium ion microscopy: A comparison of image processing techniques," *Microscopy and Microanalysis*, vol. 22, no. 5, pp. 939–947, Oct. 2016.

[6] Anders J. Barlow, Naoko Sano, Billy J. Murdoch, Jose F. Portoles, Paul J. Pigram, and Peter J. Cumpson, "Observing the evolution of regular nanostructured indium phosphide after gas cluster ion beam etching," *Applied Surface Science*, vol. 459, pp. 678–685, 2018.

[7] S. Liu, L. Sun, J. Gao, and K. Li, "A fast curtain-removal method for 3D FIB-SEM images of heterogeneous minerals," *Journal of Microscopy*, vol. 272, no. 1, pp. 3–11, 2018.

[8] T. Ott, D. Roldán, C. Redenbach, K. Schladitz, M. Godehardt, and S. Höhn, "Three-dimensional structural comparison of tantalum glancing angle deposition thin films by FIB-SEM," *Journal of Sensors and Sensor Systems*, vol. 8, no. 2, pp. 305–315, 2019.

[9] Minxu Peng, John Murray-Bruce, Karl K. Berggren, and Vivek K Goyal, "Source shot noise mitigation in focused ion beam microscopy by time-resolved measurement," *Ultramicroscopy*, vol. 211, pp. 112948, 2020.

[10] Minxu Peng, John Murray-Bruce, and Vivek K Goyal, "Time-resolved focused ion beam microscopy: Modeling, estimation methods, and analyses," *IEEE Trans. Computational Imaging*, vol. 7, pp. 547–561, 2021.

[11] Luisa Watkins, "Mitigating current variation in particle beam microscopy," arXiv:2106.04686 [eess.IV], June 2021.

[12] S. Yamada, T. Ito, K. Gouhara, and Y. Uchikawa, "Electron-count imaging in SEM," *Scanning*, vol. 13, no. 2, pp. 165–171, 1991.

[13] Liang Jin, Anna-Clare Milazzo, Stuart Kleinfelder, Shengdong Li, Philippe Leblanc, Fred Duttweiler, James C. Bouwer, Steven T. Peltier, Mark H. Ellisman, and Nguyen-Huu Xuong, "Applications of direct detection device in transmission electron microscopy," *J. Structural Biology*, vol. 161, no. 3, pp. 352–358, 2008.

[14] G. McMullan, S. Chen, R. Henderson, and A. R. Faruqi, "Detective quantum efficiency of electron area detectors in electron microscopy," *Ultramicroscopy*, vol. 109, no. 9, pp. 1126–1143, 2009.

[15] K. S. Sim, J. T. L. Thong, and J. C. H. Phang, "Effect of shot noise and secondary emission noise in scanning electron microscope images," *Scanning*, vol. 26, no. 1, pp. 36–40, 2004.

[16] John A. Notte, "Imaging with helium ions – A new detector regime with new challenges and new opportunities," American Vacuum Society 60th Int. Symp. Exhibit., Oct. 31 (presented, no proceedings), 2013.

[17] John A. Notte, Stephen Carousso, and Billy W. Ward, "Ion beam imaging," World Intellectual Property Organization publication WO 2009/079195 Al, 25 June 2009.

[18] R. M. Corless, G. H. Gonnet, D. E. G. Hare, D. J. Jeffrey, and D. E. Knuth, "On the Lambert W function," *Advances in Computational Mathematics*, vol. 5, no. 1, pp. 329–359, Dec. 1996.

[19] Thermo Fisher Scientific, "FIB nanotexture image," `https://www.fei.com/uploadedImages/FEISite/Content/Image_Gallery/Images/FIB_042(1).jpg`.

[20] Thermo Fisher Scientific, "SEM orchid lip image," `https://www.fei.com/uploadedimages/FEISite/Content/Image_Gallery/Images/2014_Image_Contest/IM_20141031_MdNasir_64_OrchidLip.jpg`.

[21] Thermo Fisher Scientific, "SEM honeycombs image," `https://www.fei.com/uploadedImages/FEISite/Content/Image_Gallery/Images/2012_Image_Contest/FEI/IM_20121011_Leuthold_84_Honeycombs_lg.jpg`.

[22] Thermo Fisher Scientific, "SEM diatome image," `https://www.fei.com/uploadedImages/FEISite/Content/Image_Gallery/Images/2012_Image_Contest/FEI/IM_20121019_ERDOGAN_33_Net_lg.jpg`.

[23] John Notte, Bill Ward, Nick Economou, Ray Hill, Randy Percival, Lou Farkas, and Shawn McVey, "An introduction to the helium ion microscope," in *AIP Conference Proceedings*. AIP, 2007, vol. 931, pp. 489–496.

[24] Yinghong Lin and David C. Joy, "A new examination of secondary electron yield data," *Surface Interface Analysis*, vol. 37, no. 11, pp. 895–900, 2005.